1. INTRODUCTION

1.1 Literature overview

1.1.1 Protein misfolding diseases – General Aspects

Despite manifold etiologies and symptoms, protein misfolding diseases (PMD) have one thing in common: the misfolding of a specific protein. The physiological function of a protein does not only depend on the amino acids it is made of but also on its three dimensional structure. Therefore, correct folding is crucial. In a post translation process, the amino acid chain gets folded by the help of other specific proteins, chaperones, into the protein's tertiary structure, composed of sheets, helices, turns, loops and other. However, in some cases, this folding process causes proteins to fold improperly. With the help of another protein, ubiquitin, the misfolded protein gets degraded and recycled. Therefore, some protein misfolding diseases are characterized by the absence of a specific protein, for example cystic fibroses, the Marfan syndrome, Gaucher's and Fabry disease. The emphasis of this thesis, however, is on a second group of diseases within the PMD that are not caused by the absence of a protein but rather by its deposition in insoluble aggregates (plaques) within the cell. These protein plaques are found to consist of amyloid fibrils, polymerized cross- β-sheet structures with the β-strands arranged perpendicular to the long axis of the fiber (Glenner, 1980; Blake & Serpell, 1996). Representatives of this type of PMD are Alzheimer's disease, Parkinson's disease, type II diabetes and members of the transmissible spongiform encephalopathies (TSE), which will be described in detail in the next chapter.

1.1.2 Transmissible spongiform encephalopathies

Transmissible spongiform encephalopathies (TSE), also termed prion diseases, are rare neurodegenerative disorders of the central nervous system. They are characterized by the accumulation of a β-sheet rich protein, the misfolded prion protein or PrP^{Sc}. A unique feature of this family is the fact that they can occur sporadically, but may also have genetic and infectious origins. The most prominent prion disease in humans is Creutzfeldt-Jakob disease (CJD), named after two German neurologists, Hans Gerhard Creutzfeldt and Alfons Maria Jakob, who first described the disorder (Creutzfeldt, 1920; Jakob, 1921). In the 1960s, it was thought that TSEs

were caused by a "slow virus", a term created by Bjorn Sigurdsson in 1954 (Sigurdsson, 1954), although no viral nucleic acid has been identified to date. Thus, in 1976, the Nobel Prize for medicine was given to Gajdusek, a supporter of this slow virus theory. Later, the possibility that the infectious agent might be a virino, a small informational molecule – most likely a piece of nucleic acid – encapsulated inside a protein coat was discussed (Kimberlin, 1982). Although this hypothesis explained most of the features found for TSE, like extreme resistance to treatments that normally destroy nucleic acids, such as ultraviolet (UV) and ionizing radiation (Alper *et al.*, 1967), no nucleic acid could be found even after 30 years of intense research. Based on a theoretical work from 1967, where it was suggested that the agent might be a protein (Griffith, 1967), Stanley Prusiner and colleagues isolated the protease resistant prion protein (PrP^{res}) from infectious material (Bolton *et al.*, 1982), and a crucial step in understanding the nature of the new infectious agent was made. This discovery finally earned him the Nobel Prize for Medicine in 1997. Since there is no therapy available to date, all TSEs eventually result in death.

1.1.2.1 Human prion diseases

Human prion diseases can present as sporadic, iatrogenic and inherited diseases and consist of different types of Creutzfeldt-Jakob disease, Kuru, the Gerstmann-Sträussler-Scheinker syndrome and fatal familial insomnia. They are rapidly progressing disorders of the central nervous system involving the formation of amyloid plaques.

Creutzfeldt-Jakob disease (CJD)

Although only affecting about 1 person per million people per year, CJD is the most prominent prion disease among human TSEs. Named after two German neurologists, Creutzfeldt and Jakob, this type of TSE can occur sporadically, inherited and infectious (Gambetti *et al.*, 2003). Its transmissibility was shown by successful infection of chimpanzees in the 1960's (Gibbs *et al.*, 1968). It occurs in almost equal ratios between the sexes, although males of the age 60 or older appear to have a higher incidence of disease (Holman *et al.*, 1996; Gibbons *et al.*, 2000). Affected patients usually present with a rapidly progressive dementia, visual abnormalities, or cerebellar dysfunction, including muscle incoordination and gait and speech abnormalities. The median illness is about 4 months (mean: 7.6 months) with death

occurring within 12 months of illness onset in ~85-90% of patients (Brown *et al.*, 1986). There are currently four known strains that are associated with distinct types of sporadic or acquired CJD: sporadic, familial, iatrogenic, and variant CJD.

In sporadic CJD, which comprised about 85% of all CJD cases, only ~5-10 % of the patients show plaques (DeArmond, 2000). According to the two proposed hypotheses about the origin of sporadic CJD (Prusiner, 1996), it could be caused either by an age-related mutation in the prion protein gene or by spontaneous conversion of PrP^{C} into PrP^{Sc} in a single neuron or a group of neurons, initiating a chain reaction that results in the spread of disease to other susceptible neurons.

The familial or inherited form of CJD occurs in about 5-15% of cases. It is most frequently associated with mutations at codon 200 (and to a smaller extend at codons 178, 183, 208 or 210) of the prion protein gene (Brown *et al.*, 1991; Furukawa *et al.*, 1996; Gajdusek, 1996; Ghetti *et al.*, 1996; Goldfarb *et al.*, 1992; Goldfarb *et al.*, 1991; Pocchiari *et al.*, 1993).

In 1974, a person to person transmission of the CJD agent was shown when a 55–year-old patient developed the disease 18 months after receiving a corneal transplant obtained from a donor with CJD (Duffy *et al.*, 1974). Other modes of iatrogenic transmission were then reported, including the use of contaminated EEG depth electrodes (Bernoulli *et al.*, 1977), neurosurgical instruments (Will & Matthews, 1982), cadaveric pituitary-derived gonadotropin (Cochius *et al.*, 1990; Cochius *et al.*, 1992), and dura mater grafts (Thadani *et al.*, 1988). It has been shown that the human prion protein gene exhibits a polymorphism for methionine or valine at codon 129. Persons who are homozygous for either one of these seem to be predisposed to developing iatrogenic (or sporadic) CJD while heterozygosity seems to be protective against both forms of CJD (Brown *et al.*, 1994; Collinge *et al.*, 1991; Deslys *et al.*, 1994; Palmer *et al.*, 1991).

In 1996 the first case of a new variant form of CJD (vCJD), the clinical and neuropathological profiles of which were found to be noticeably different from sporadic CJD, was described in a patient younger than 40 years old in the UK. In contrast to the other forms, vCJD exhibits high levels of PrP-containing plaques (Ironside, 2000). Between February 1994 and October 1995 a total of ten cases of Creutzfeldt-Jakob disease in unusually young patients, ranging in age from 16-39 years, were recognized. The clinical and neuropathological features of these ten cases were described in detail by Will and colleagues, revealing unusual features like

prominent behavioral changes at the time of clinical presentation, with subsequent onset of neurological abnormalities, including ataxia within weeks or months, dementia and myoclonus late in the illness and nondiagnostic EEG changes (Will *et al.*, 1996). On March 20, 1996, the UK government's expert advisory committee announced its conclusion that the agent causing BSE might have spread to humans. As of February 1999, 38 confirmed and 2 probable cases had been reported with an age of onset ranging from 16 to 52 years with a median age of 28 years (Zeidler *et al.*, 1997). All of these patients were tested and were homozygous for methionine at codon 129 (Zeidler *et al.*, 1997). From 1995 to date (as of April, 2nd 2007), 159 suspected vCJD cases were reported in the United Kingdom with 112 of them confirmed (http://www.cjd.ed.ac.uk/figures.htm).

Kuru

Transmitted by ritual cannibalism, Kuru occurred at epidemic levels in the 1950s-60s among aborigines in Papua New Guinea (Gajdusek, 1977). The ritual involved the consuming of and rubbing the face with nervous tissue from dead relatives as a sign of respect. The disease was also called the "laughing death" because the patient's emotions could switch from sadness to happiness with sudden outbursts of laughter. Early symptoms include loss of muscle coordination which resulted in difficulties of walking as well as tremor and shivering. The terminal stage is characterized by an inability to sit up without support, incontinence, dysphagia and ataxia and leads to death after about 3 to 24 month of illness. Historically, similarities between Kuru and the oldest known TSE, Scrapie, at the clinical, neuropathological and epidemiological levels lead to the suggestion that Kuru may also be transmissible (Klatzo *et al.*, 1959; Hadlow, 1995). This was proven by successful transmission to chimpanzees in the 1960's (Gajdusek *et al.*, 1966). By governmental prohibition of the cannibalistic ritual, Kuru has been virtually eliminated.

Gerstmann-Sträussler-Scheinker syndrome

About 100 fold less common than CJD, the Gerstmann-Sträussler-Scheinker syndrome (GSSS), caused by a mutation in the PRNP gene, occurs worldwide in men between ages 40 – 60 years. In GSSS, the life expectancy (~5 years) is considerably longer than for CJD, where patients die about 6 - 9 months after the onset of symptoms. The most common but not sole mutation is the substitution of proline by

leucine at codon 102 (P102L) (Hsiao *et al.*, 1989; Doh-ura *et al.*, 1989; Goldgaber *et al.*, 1989). It was first described in 1936 by Gerstmann, Sträussler and Scheinker (Richardson & Masters, 1995), being considered a variant of the familial form of CJD but being primarily associated with mutations at codon 102 and less frequently with mutations at codon 105, 117, 145, 198 or 217 of the prion protein gene (Gajdusek, 1996). Cerebellar ataxia, dementia, ocular dysmetria, hyporeflexia or areflexia in the lower extremities, gait abnormalities and dysarthria are commonly reported neurological signs and symptoms in GSSS (Kretzschmar, 1993).

Fatal Familial Insomnia

As the GSSS, fatal familial insomnia is an autosomal dominant disorder. It is caused by a mutation in the prion protein gene and has been found in only 28 families worldwide, including cases in Australia, Austria, Britain, France, Germany, Italy, Japan and the United States (Bosque *et al.*, 1992; Gambetti & Lugaresi, 1998; McLean *et al.*, 1997; Medori *et al.*, 1992b; Nagayama *et al.*, 1996; Reder *et al.*, 1995; Rossi *et al.*, 1998). The mutation, in which asparagine-178 is replaced by aspartic acid (Medori *et al.*, 1992a; Little *et al.*, 1986), causes the protein to fold into the pathogenic form and accumulate forming plaques in the thalamus, the region of the brain which regulates sleep (Manetto *et al.*, 1992). Starting with insomnia, during progression of the disease, patients experience hallucinations leading to panic attacks and weight loss. After about a year, patients suffer from dementia and eventually die. Although typically a hereditary disease, several sporadic cases have been identified (sporadic fatal insomnia). Neither the sporadic nor the familial form exhibit plaques (Budka *et al.*, 1995; DeArmond, 2000; Manetto *et al.*, 1992).

1.1.2.2 Animal prion diseases

Although it seems that almost all mammals are susceptible to prion diseases, there are only six known disorders so far: scrapie, bovine spongiform encephalopathy (BSE), transmissible mink encephalopathy (TME), chronic wasting disease (CWD), feline spongiform encephalopathy (FSE) and spongiform encephalopathies of zoo animals (EUE).

Scrapie

Scrapie is the oldest known prion disease; it has been first described in 1732 in sheep (McGowan, 1922). The name "Scrapie" was derived from the observation that due to intense itchiness the animals scrape off their coat. Other symptoms include jumpiness, excessive loss of weight, tremor, loss of coordination and behavioral changes. In 1934, scrapie was accidentally proven to be an infectious disease by injecting diseased sheep brain into healthy sheep (Cuille & Chelle, 1936). In 1939, it was shown that it is also infectious to goats (Cuille & Chelle, 1939). Later, its transmissibility was proven experimentally in 1960, when Chandler succeeded in transmitting the disease to mice (Chandler, 1961). Since then, mice and hamsters were used as models to study the pathogenesis of scrapie (Kimberlin & Walker, 1988). In sheep, the incubation time is at least 1 year (Gibbons & Hunter, 1967) followed by a clinical stage of about four to nine month, which is usually longer than in goats (Andrews *et al.*, 1992). Today it is believed that the horizontal spread of scrapie is caused by the consumption of infected placenta (Brotherston *et al.*, 1968; Brotherston *et al.*, 1968; Dickinson *et al.*, 1974). In contrast to mad cow disease, amyloid plaques are seen only seldom (Wood *et al.*, 1997). Amyloid plaques are seen only seldom (Somerville *et al.*, 1997).

Bovine Spongiform Encephalopathy

In 1986, a new spongiform encephalopathy was recognized in cattle in Great Britain, where it caused a large outbreak (Wells *et al.*, 1987). The affected cows were thought to have been infected by exposure with the agent through food in the early 1980s. To enrich the diet of cattle, meat-and-bone meal had been added to feed and probably carried the infectious agent. This enrichment was banned by the British government in July 1988 to constrict the spread of the disease. As of January 26th, 2007, there are more than 190.000 reported cases of BSE worldwide, 97% of which occurred in the United Kingdom, with a vast majority reported in Great Britain (www.oie.int/eng/info/en_esbmonde.htm). One year after the discovery of variant CJD (vCJD), Hill et al. proved that BSE and vCJD were caused by the same prion strain, and concluded that the consumption of BSE-contaminated food is the most likely cause of vCJD in humans (Hill *et al.*, 1997). In contrast to scrapie, amyloid plaques are a common histopathological feature (Wood *et al.*, 1997).

Chronic Wasting Disease

Chronic wasting disease (CWD) was first identified in the late 1960s in captive mule deer in a wildlife research facility in the US state of Colorado. It remained limited to captive deer until 1981, but in the 1990s it also occurred in free-ranging mule deer (*Odocoileus hemionus*), white tail deer (*Odocoileus virginianus*) and Rocky Mountain elk (*Cervus elaphus nelsoni*) in the US states Colorado (northeastern part) and Wyoming (southeastern part) (Williams & Young, 1992), and together with western Nebraska. It later was also found (Williams & Miller, 2002), these states form the endemic area and was recognized as a transmissible spongiform encephalopathy in 1978 (Williams & Young, 1980). In 2006, the area has expanded to a total of six states, including Utah (first confirmed case in 2003), South Dakota and Kansas. To date, it has also been detected in captive cervids in Illinois, New Mexico and New York (O'Rourke, 2005) and the Canadian provinces of Alberta and Saskatchewan. Its increasing number raised the concern of a possible risk to humans. However, non-domestic ruminants like the pronghorn antelope, moose, the Rocky Mountain bighorn sheep and mountain goats have been in contact with CWD-affected deer and elk but have not developed the disease (Williams & Young, 1992). So far, transmission could only be shown experimentally: in sheep (Hamir *et al.*, 2006a), transgenic mice expressing elk prion protein (Kong *et al.*, 2005), ferrets, mink, squirrel monkeys, goats (Williams & Miller, 2002; Marsh *et al.*, 2005; Bartz *et al.*, 1998) and partly cattle (Hamir *et al.*, 2006c; Hamir *et al.*, 2005). Addititional in vitro studies showed that the possible risk of transmission to human, cattle, and sheep is probably low (Raymond *et al.*, 2000). PrP^{CWD} was immunohistochemically found in brain, spinal cord, eyes, peripheral nerves and lymphoreticular tissues (Spraker *et al.*, 2002; Sigurdson *et al.*, 2001). Interestingly, CWD is the only TSE known to affect free-ranging wildlife species. Four hypotheses have been proposed regarding its origin, while one of them, the infection of deer by a strain of scrapie that has adapted to cervids, might be considered the most commonly accepted theory (Salman *et al.*, 2003).

TME, FSE and spongiform encephalopathies in zoo animals (EUE)

First described in 1947 in a farm in Wisconsin, transmissible mink encephalopathy (TME) is a rare sporadic disease of ranch-raised adult mink. Later, cases were also reported in Canada, Finland, Russia and the former German Democratic Republic (Marsh *et al.*, 1991). The clinical signs include loss of cleanliness, confusion,

drowsiness and aimless circling. Transmissibility could be shown by intracerebral inoculation to raccoons in 2004 (Hamir *et al.*, 2004), and cattle (in 2006) (Hamir *et al.*, 2006b). It was believed that the ranch animals got infected by scrapie contaminated food (Hartsough & Burger, 1965), but to date it is more likely that the consumption of BSE derived food was the cause for this type of disease, that was last reported in the US in 1985 (Marsh *et al.*, 1991).

Feline spongiform encephalopathy (FSE) is another type of prion disease believed to be caused by BSE contaminated food. It was first reported in 1990 in a domestic cat in Great Britain (Wyatt *et al.*, 1991) and later also in other countries like Norway (Bratberg *et al.*, 1995) and Italy, where it occurred simultaneously in a cat and its owner (Zanusso *et al.*, 1998).

Exotic ungulate encephalopathies (EUE) are discovered in 1986 in antelopes in zoos in the UK who showed the same symptoms as BSE infected cattle. In 1992, prion diseases were also discovered in large cats like pumas, lions and tigers of zoos in the United Kingdom. In 1996, a zoo in Montpellier, France, reported of TSE cases in nonhuman primates. All these encephalopathies are believed to be caused by the consumption of BSE contaminated food.

Table 1.1: Overview of the human and animal prion diseases (adapted from (Nunziante, 2003; Aguzzi *et al.*, 2004))

Host		Disease	Cause	First described
Animal	Sheep / Goat	Scrapie	vertical and horizontal infection in genetically susceptible sheep; oral transmission; sporadic	1732 (McGowan, 1922)
	Cattle	BSE (bovine spongiform encephalopathy)	Infection with prion-contaminated food; sporadic (?)	1987 (Wells *et al.*, 1987)
	Deer, Elk	CWD (chronic wasting disease)	Unclear, possibly similar to Scrapie	1980 (Williams & Young, 1980)
	Mink	TME (transmissible mink encephalopathy)	Infection with contaminated meat from sheep and cattle	1992 (Marsh & Hadlow, 1992)
	Cat	FSE (feline spongiform encephalopathy)	Infection with contaminated bovine tissue and food	1991 (Wyatt *et al.*, 1991)
	Zoo animals	EUE (exotic ungulate encephalopathy)	Ingestion of BSE-contaminated feed (infection)	1988 ;
Human		Kuru	Acquired through cannibalistic rituals	1955-1957 (Gajdusek & Zigas, 1957)
		CJD (Creutzfeldt-Jakob disease) - Familial	Inherited (mutation in the PRNP gene)	1930 (Meggendorfer , 1930)
		- Sporadic	Spontaneous conversion of PrP^{C} into PrP^{Sc} (?) Somatic PRNP mutation (?)	1920 (Creutzfeldt, 1920)
		- Iatrogenic	Acquired from contaminated instruments, dura mater grafts or growth hormone (infection)	1974 (Duffy *et al.*, 1974)
		- vCJD (variant CJD)	Acquired (infection by bovine prions)	1996 (Will *et al.*, 1996)
		GSSS (Gerstmann-Sträussler-Scheinker syndrome)	Inherited (mutation in the PrP gene)	1936 (Gerstmann *et al.*, 1936)
		FFI (fatal familial insomnia)	Inherited (mutation in the PrP gene)	late 1970's

1.1.2.3 The prion protein: PrP^{C} and PrP^{Sc}

The causative agent of TSE is believed to be a protein, the so-called prion, a proteinaceous infectious particle that lacks agent-specific nucleic acid (Prusiner, 1997). Over the past years, experimental evidence supporting this spectacular hypothesis has accumulated. Soto and colleagues, for example, generated infectious scrapie prions in vitro (Castilla *et al.*, 2005) and Kretzschmar and colleagues

performed in vitro protein misfolding cyclic amplification (PMCA) experiments (Bieschke *et al.*, 2004). A major feature that distinguishes prions from viruses is that the non-pathogenic form of prions is encoded by a chromosomal gene (Prusiner, 1998), the PRNP gene, which is located on chromosome 20 in humans (Robakis *et al.*, 1986). Despite an identical amino acid sequence, the prion protein can exist in different secondary (and tertiary) structures. PrP^{C}, the cellular prion protein, is a GPI anchored glycosylated protein that is mainly expressed in neurons, but also in glia of the brain and spinal cord, as well as in several peripheral tissues and in leukocytes (Bendheim *et al.*, 1992; Caughey *et al.*, 1988; Moser *et al.*, 1995; Manson *et al.*, 1992; Harris *et al.*, 1993; Dodelet & Cashman, 1998). PrP^{C} is mainly but not exclusively expressed by neuronal cells (Kretzschmar *et al.*, 1986a), is high in α-helix (42%), whereas the misfolded or disease-associated form (Scrapie prion protein or PrP^{Sc}) shows a high amount of β-sheet structures (43%) and has less α-helix (30%) (Pan *et al.*, 1993). In Syrian hamsters, PrP^{C} is composed of 254 amino acids in its unprocessed form (Basler *et al.*, 1986). The signal sequence represented by amino acids 1-22 is truncated together with amino acids 232-254, resulting in the native prion protein. In comparison, the human PrP has 253 amino acids and shows 90% similarity to hamster PrP (Kretzschmar *et al.*, 1986b). The two isoforms, PrP^{C} and PrP^{Sc}, not only differ in their secondary structure but also in their biochemical properties. PrP^{Sc} is insoluble in detergents (Meyer *et al.*, 1986), resistant against heat and only partially degradable by proteinase K (Bolton *et al.*, 1982; Oesch *et al.*, 1985). It forms fibrils and accumulates in the CNS, which is not the case for PrP^{C}. NMR structures of the recombinant human prion protein, hPrP(23-230) have shown that the protein consists of a C-terminal globular domain extending from residues 125-228 and an N-terminal flexibly disordered part. The globular domain is composed of the α-helices and two short β-strands flanking the first α-helix (Zahn *et al.*, 2000).

The function of PrP is not fully understood yet. Recently, neuroprotective and antiapoptotic effects of the cellular prion protein were demonstrated (Chiarini *et al.*, 2002; Roucou *et al.*, 2003; Roucou *et al.*, 2005). PRNP knock-out mice ($PrP^{o/o}$) do not have a particular phenotype (Bueler *et al.*, 1992), but are completely resistant against prion inoculation and do not “replicate” the protein (Bueler *et al.*, 1993). However, they exhibit some electrophysiological and structural abnormalities in the hippocampus (Collinge *et al.*, 1994; Colling *et al.*, 1996; Colling *et al.*, 1997; Manson *et al.*, 1995; Whittington *et al.*, 1995), loss of cerebellar Purkinje cells (Sakaguchi *et al.*,

1996), changes in learning and memory (Nishida *et al.*, 1997), alterations in circadian rhythms and sleep (Tobler *et al.*, 1996), as well as a reduced Cu^{2+} content (up to 50%) in membrane preparations (Brown *et al.*, 1997b) in comparison to wild type mice, arguing for a role of PrP in copper metabolism and trafficking. In addition to copper ions (Brown *et al.*, 1998; Pauly & Harris, 1998; Viles *et al.*, 1999), PrP^C also binds zinc, manganese, and nickel cations, although with lower affinities than for copper (Pan *et al.*, 1992; Brown *et al.*, 2000; Jackson *et al.*, 2001). Most probably, the membrane-bound PrP^C seems to play a role in signal transduction (Mouillet-Richard *et al.*, 2000; Reilly, 2000), cell survival and differentiation (Chen *et al.*, 2003; Santuccione *et al.*, 2005). Indeed, there is evidence that the presence of PrP^C that can not be converted into PrP^{Sc} prevents the neurodegenerative effects of non-host specific PrP^{Sc} (Raeber *et al.*, 1997)

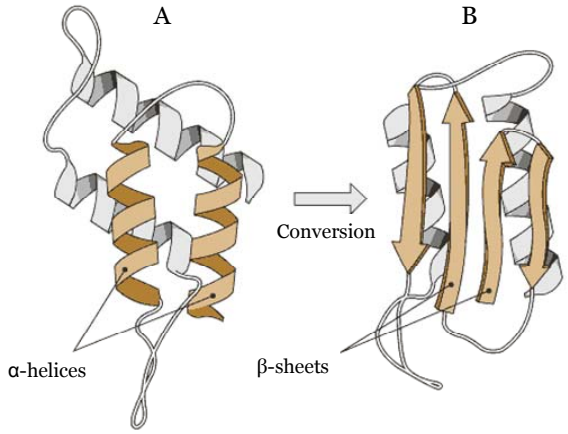

Figure 1.1: secondary structure of PrP^C (A) and PrP^{Sc} (B). Helices in PrP^C shown in brown get transformed into β-sheet by conversion to PrP^{Sc}. From (Prusiner, 1999)

1.1.2.4 Conversion of PrP^C to PrP^{Sc}

Two hypotheses have been proposed for the conversion of the cellular into the pathogenic form of the prion protein, the heterodimer and the seed polymerization model, also termed nucleated polymerization model. According to the heterodimer hypothesis (Prusiner, 1982; Cohen *et al.*, 1994), the cellular prion protein of a host is converted into PrP^{Sc} by partial unfolding into a transitional state designated as PrP^*; PrP^* then refolds under the influence of PrP^{Sc}, resulting in a homodimer complex, possibly along with a hypothetical molecular chaperone (Prusiner, 1998). The newly generated PrP^{Sc} will then induce conversion of another PrP^C molecule in an autocatalytic process. A recent study has shown that PrP^C's C-terminal α-helices are

conserved in PrP^{Sc}, whereas secondary structural changes are located in the N-terminal α-helix (Eghiaian *et al.*, 2004). According to the second existing hypothesis, the seed polymerization model, PrP always also exists in the form of PrP^{Sc}, although only in small amounts and for short periods. This molecule stabilizes by the aggregation of multiple short term molecules and in this way builds the base for more molecules to convert. Then, when an aggregate of these PrP^{Sc} molecules comes in contact with PrP^{C}, it is converted into PrP^{Sc} and added to the growing aggregate (Caughey, 2001; Jarrett & Lansbury, 1993; Caughey *et al.*, 1997; Deignan *et al.*, 2004; Gajdusek, 1994a; Gajdusek, 1994b; Harper & Lansbury, 1997).

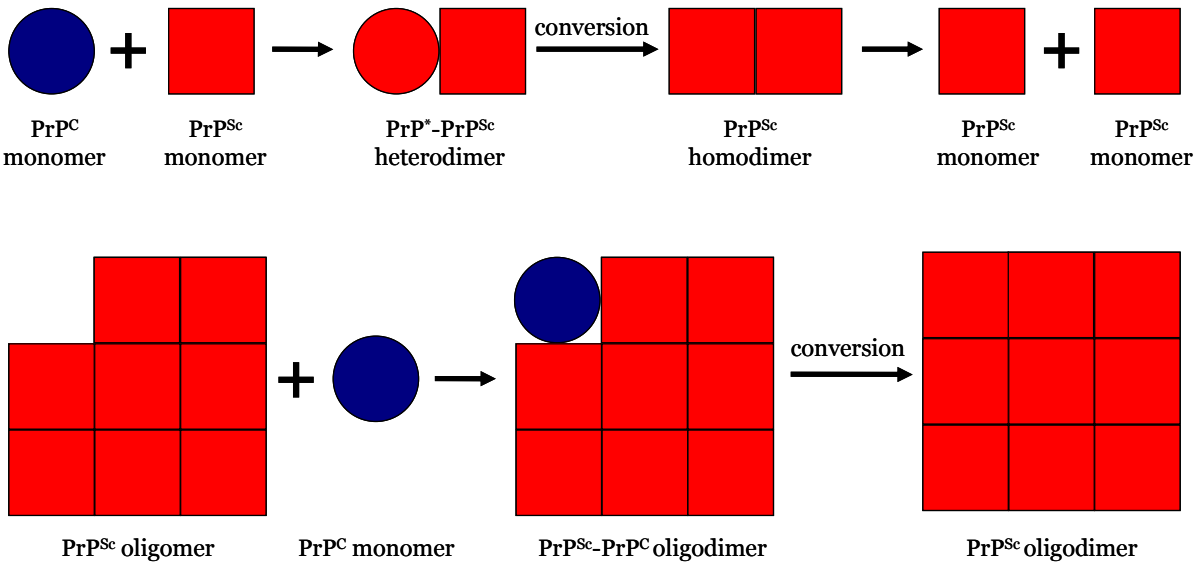

Figure 1.2: simplified illustration of the two proposed hypotheses for prion conversion. A. heterodimer hypothesis: a PrP^{C} monomer attachs to a PrP^{Sc} monomer, building a PrP^{Sc}-PrP* heterodimer before getting converted into PrP^{Sc} and separating into PrP^{Sc} monomers. B. seed polymerization model: PrP always also exist in form of PrP^{Sc}. This status stabilizes by aggregation of multiple of these short term molecules and in this way build the base for more molecules to convert, so that an aggregate of these PrP^{Sc} molecules gets in contact with a PrP^{C}, which gets converted into PrP^{Sc} and added to the so growing aggregation. Adapted from http://www.udel.edu/chem/bahnson/chem645/websites/Janas/

1.1.2.5 Prion Strains

When isolates from scrapie diseased sheep were first passaged into goats, the animals exhibited different symptoms, separating them into two distinct groups (Brotherston *et al.*, 1968): “drowsy” and “scratching”. They are now known as different strains, whose molecular basis was proposed to be PrP^{Sc} polymers with distinct three-dimensional structures (Bessen *et al.*, 1995). It was shown that proteinase K splits these two prion proteins at different locations (Bessen & Marsh, 1994). To date, more

than 20 phenotypically different strains were identified after passaging scrapie through mice (Bruce, 1993). When infection occurs under defined conditions, strains are reproducible in incubation time (Dickinson, 1977), lesion profiles and PrP^{Sc} deposition (Hecker *et al.*, 1992; Prusiner, 1997), host range (Kimberlin & Walker, 1978), PK resistance (Bessen & Marsh, 1992a; Bessen & Marsh, 1992b; Bessen & Marsh, 1994) and symptoms (Carp *et al.*, 1984). Considerable evidence today indicates that the diversity of prion strains may be encoded within the prion protein itself and it is now known that distinct PrP^{Sc} conformations (Caughey *et al.*, 1998), molecular weight and patterns of glycosylation (Hill *et al.*, 1997; Somerville *et al.*, 1997; Kuczius *et al.*, 1998; Collinge *et al.*, 1996) are associated with different prion strains. In addition, strains are distinguishable by antibody affinity (Stockel *et al.*, 1998). In mice, the incubation period of different TSE depends on genetic factors of the host (Kingsbury *et al.*, 1983) as well as on the strain (Bruce & Dickinson, 1987). Not only in mice, the incubation period is also used in hamsters to differentiate between distinct prion strains (Lowenstein *et al.*, 1990; Thomzig *et al.*, 2004; Marsh & Kimberlin, 1975; Marsh & Kimberlin, 1975). Recently, FTIR spectroscopy was used to distinguish between different TSE strains in hamsters (Thomzig *et al.*, 2004; Spassov, 2006; Caughey *et al.*, 1998) and mice (Silveira *et al.*, 2004).

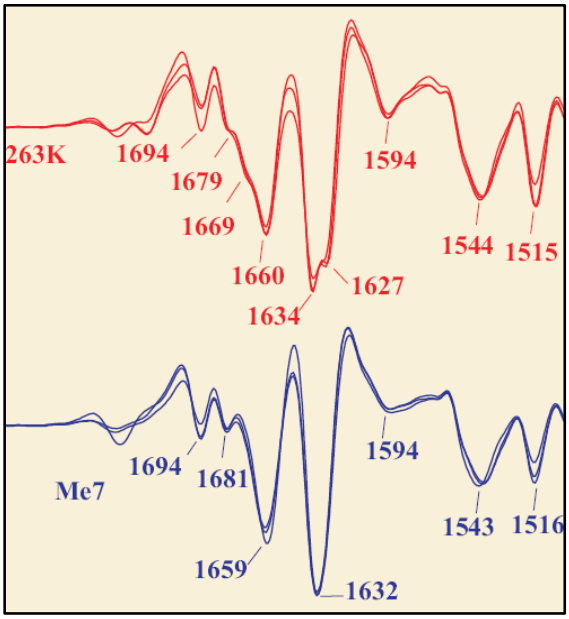

Figure 1.3: PrP27-30 second derivative spectra in the amide sensitive spectral ranges- amide I and amide II obtained from two different TSE strains in dried samples. The spectra have been normalized between 1750 and 1600 wavenumbers. The overlaid spectra represent measurements of samples purified in independent extraction and purification procedures. From (Spassov, 2006)

1.1.2.6 Metals in prion diseases

There is increasing evidence that metals are involved in the pathogenesis of protein misfolding diseases such as Alzheimer's disease (Smith *et al.*, 1997; Nunomura *et al.*, 2004; Nunomura *et al.*, 1999a; Nunomura *et al.*, 1999b) and other neurodegenerative disorders (Perry *et al.*, 2002; Sayre *et al.*, 2000).

The relation of *copper* and the cellular prion protein, as well as its influence on the conversion to the misfolded form has been studied most. It has been shown that the cellular prion protein binds copper in vivo (Brown *et al.*, 1997a; Todorova-Balvay *et al.*, 2005). However, to date, different opinions about its role in prion pathogenesis exist. While some researchers claim that copper inhibits or delays the onset of disease (Sigurdsson *et al.*, 2003; Orem *et al.*, 2006; Ricchelli *et al.*, 2006; Cox *et al.*, 2006), others describe a deleterious function (Kim *et al.*, 2005), showing that, in vitro, copper converts PrP^{C} into a protease resistant form (Quaglio *et al.*, 2001) and more PrP^{Sc} are formed (Kim *et al.*, 2005). These in vitro experiments lead to the hypothesis that Cu^{2+} ions might regulate the pathogenesis of prion diseases in vivo (Orem *et al.*, 2006), for example the regulation of PrP^{C} mRNA expression, if presented extracellularly (Toni *et al.*, 2005; Varela-Nallar *et al.*, 2006). Additionally, it was shown that when copper levels are disturbed, central nervous system disorders are prevalent (Camakaris *et al.*, 1999).

Similarly to that, the *iron* regulation was shown to be disturbed in scrapie infected mouse neuroblastoma cells (Fernaeus *et al.*, 2005; Fernaeus & Land, 2005), showing decreased intracellular levels. In GSSS and vCJD, iron could be found in the majority of cored prion protein deposits. Ferritin, the iron storing protein, has also been found to be heavily deposited in both the PrP lesions and surrounding cells (Petersen *et al.*, 2005). It has recently been shown to be co-transported with PrP^{res} (Mishra *et al.*, 2004).

In addition to copper, the octapeptide repeat sequences in the N-terminus of PrP^{C} also binds *zinc* and manganese, albeit at a lower affinity (Wong *et al.*, 2001b). Zn^{2+} was shown to promote organization of human PrP aggregates into well structured, amyloid-like fibrillar filaments (Ricchelli *et al.*, 2006). In CJD brains Zinc, copper and manganese levels were shown to change (Wong *et al.*, 2001a).

The presence of *manganese* also leads to the conversion of PrP^{C} into the abnormal form and increased resistance of PrP^{C} to proteinase K digestion (Brown *et al.*, 2000);

(Choi *et al.*, 2006). Kim and colleagues used modified PMCA (protein misfolding cyclic amplification) and showed an increase of PrP^{res} after mixing manganese with brain homogenate containing PrP^{C} (Kim *et al.*, 2005). However, in a different study, Mn^{2+} was shown to delay the conversion of the human prion protein in the pathogenic form and even inhibit the conversion of the Gerstmann-Sträussler-Scheinker peptide into amyloid fibrils (Ricchelli *et al.*, 2006). In addition, changes in the levels of copper and manganese could be shown in the brains of scrapie-infected mice prior to the onset of clinical symptoms (Thackray *et al.*, 2002).
Despite intensive research to date, the exact role of metals in prion pathogenesis remains unclear and needs further investigation.

1.1.2.7 The scrapie-263K hamster model

The Syrian hamster (*Mesocricetus auratus*) is a suitable model to study the pathology of the Scrapie strain 263K after oral uptake due to a relatively short incubation time compared to sheep, goats or even mice (Baier *et al.*, 2003) and the possibility to investigate a large number of animals relatively easily. Attempts to transmit Scrapie to Syrian hamsters were started as early as 1965, when Zlotnik and Rennie transmitted mouse-passaged Scrapie to goats, sheep, rats, and hamsters (Zlotnik & Rennie, 1965). In 1977, Kimberlin and Walker were the first to passage Scrapie strain 263K to Mesocricetus auratus (Kimberlin & Walker, 1977). The oral route of infection is presently viewed as the most epidemiologically relevant pathway for the natural transmission of Scrapie (Diringer *et al.*, 1994). The nervous system of orally infected hamsters has been studied for the appearance of pathological prion protein (Beekes *et al.*, 1996). The pathogenetic process was observed to begin in the spinal cord between vertebrae T4 and T9, and then show an antero- and retrograde spread with a rate of 0.8-1.0 mm/day (Beekes *et al.*, 1996). These studies also revealed a possible alternate route of infection from the periphery to the brain via the spinal cord. Encouraged by this finding, a series of experiments were initiated with orally infected hamsters to unravel the route of the infectious agent to the brain (Beekes *et al.*, 1998; Baldauf *et al.*, 1997). Oral infection was achieved by feeding 3-week old hamsters one-time with food pellets soaked with brain homogenate from terminally ill hamsters. After bypassing the gut, the misfolded PrP was detected in two distinct routes terminating in the CNS: The retrograde route starts from efferent, parasympathetic fibers and ends

in the vagus nerve to the nucleus dorsalis nervi vagi (DMNV) and nucleus tracti solitarii (see schematic in **Figure 1.4**) (Beekes *et al.*, 1998). Both nuclei are located in the medulla oblongata, which is formed by the enlarged top of the spinal cord. The second route uses the efferent connections via pre-vertebral ganglia (ganglion coeliacum and ganglion mesentericum superius, CMGC) on nervus splanchnicus to the intermediolateral gray matter in the area between thoracic spinal cord segments T5-T12. From there, the spread of PrP^{Sc} continues to the corresponding afferent dorsal root ganglia (nodules on a dorsal root that contain cell bodies of afferent nerve fibers), where the protein can first be detected 76 days post-infection in half of the examined hamsters (Beekes *et al.*, 1998; McBride *et al.*, 2001; McBride & Beekes, 1999).

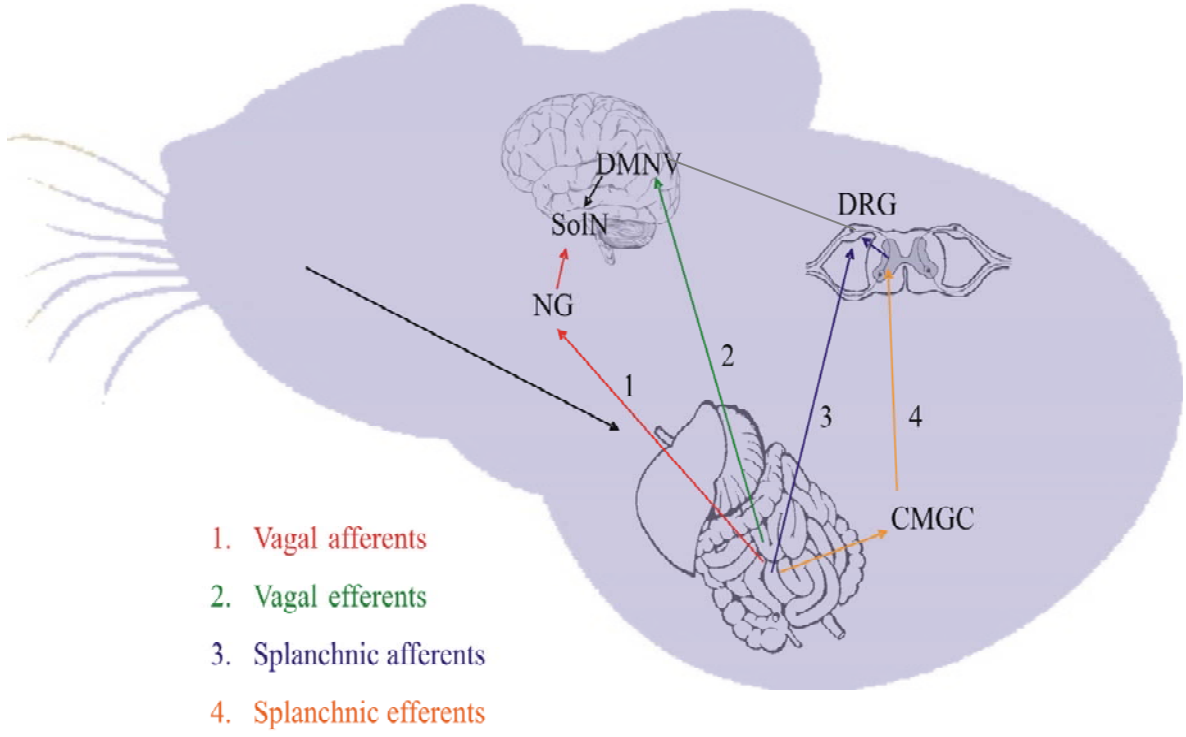

Figure 1.4: Initial spread of the 263K agent after oral uptake. Circuitry has been simplified to show major routes only. The infectious agent reaches the CNS by spreading along either efferent (motor) or afferent (sensory) fibers of vagus or splanchnic nerves. Efferent fibers of the vagus nerve have their nerve cell bodies in the dorsal motor nucleus of the vagus nerve (DMNV) and synapse with neurons of the enteric nervous system in ganglia of the submucosal and myenteric plexuses in the wall of the alimentary canal. The nerve cells of vagus nerve afferent fibers are located in the nodosal ganglion (NG) and directly innervate the alimentary canal. These fibers run to the solitary tract nucleus (SolN), where they connect to interneurons projecting to the DMNV. The cell bodies of splanchnic nerve efferent fibers are located in the IML and interrelate to neurons of the coeliac mesenteriac ganglion complex (CMGC) that, in turn, innervate the gastrointestinal tract. Afferent fibers of the splanchnic nerve originate in the DRG, run through the CMGC, and directly innervate target organs such as the alimentary canal. Enteric and abdominal ganglia (CMGC) have an early involvement in pathogenesis. Adapted from (McBride & Beekes, 1999)

1.1.3 Reovirus T3C9

Reovirus type 3 clone 9 (T3C9) is a member of the genus Orthoreovirus within the family of Reoviridae. Reoviridae infect a wide range of hosts, including vertebrates, invertebrates and plants. The name Reovirus –originally proposed by Sabin (Sabin, 1959)- was chosen because viruses of this group had been isolated from the respiratory and enteric tracts and could not be associated with a human disease ("orphan"). Meanwhile, it is known that four of the nine genera cause diseases in human, for example the Colorado tick fever virus and the human rotavirus. Recently it has been proposed that serotype 3 reoviruses can even cause meningitis in humans (Tyler *et al.*, 2004).

The genome consists of linear, segmented double-stranded RNA, ten segments in case of the Orthoreoviruses, eleven in Rotaviruses and twelve in Coltiviruses, the genera that contain human viruses. The reoviral capsid is non-enveloped and icosahedric in shape, approximately 70-80 nm in diameter (see **Figure 1.5**). Unique among viruses, reoviridae have an outer and inner capsid that surround an inner core containing necessary enzymes for mRNA synthesis, including RNA polymerase. In this way, carrying all enzymes essential for replication, reoviruses do not need to fully uncoat. Orthoreoviruses enter the host cell either by receptor mediated endocytosis (Baer *et al.*, 1999; Borsa *et al.*, 1979; Borsa *et al.*, 1981) or as a result of digestion with chymotrypsin in the intestine (Sturzenbecker *et al.*, 1987; Borsa *et al.*, 1973). In endosomes, viruses remove the outer capsid protein σ3 and cleave the outer capsid protein μ1 (Baer *et al.*, 1999; Borsa *et al.*, 1981; Sturzenbecker *et al.*, 1987; Ebert *et al.*, 2002) by proteolytic disassembly. Then, the infectious subvirion particle is capable of penetrating endosomal membranes and release the transcriptionally active viral core particle into the cytoplasm (Chandran *et al.*, 2002; Chandran *et al.*, 2003; Odegard *et al.*, 2004), where it replicates. Afterwards, virions self assemble and accumulate in inclusion bodies before they are released by cell lysis (see **Figure 1.4**).

The genus Orthoreovirus contains four species: mammalian, avian, Nelson Bay and Baboon orthoreovirus which can be divided into three distinct subgroups when comparing amino acid sequences of the α2 protein (major inner capsid). Mammalian reovirus type 3 clone 9 (T3C9) infection has been extensively studied in mice (Derrien & Fields, 2000; Tyler *et al.*, 1989; Virgin & Tyler, 1991; Barkon *et al.*, 1996; Derrien & Fields, 1999) but it was unknown whether hamster are developing an encephalopathy

too. In mice it could be shown that only neonatal but not adult animals are susceptible (Mann *et al.*, 2002; Oberhaus *et al.*, 1997; Flamand *et al.*, 1991).
In this thesis, reovirus T3C9 was chosen because it follows the same pathway after oral uptake and therefore reaches the same histological areas in the brain as the scrapie agent 263K (Morrison *et al.*, 1991). This feature made it a suitable model to examine the specificity of spectral differences found in 263K scrapie infected hamster DMNV (Kneipp *et al.*, 2000; Kneipp *et al.*, 2002).

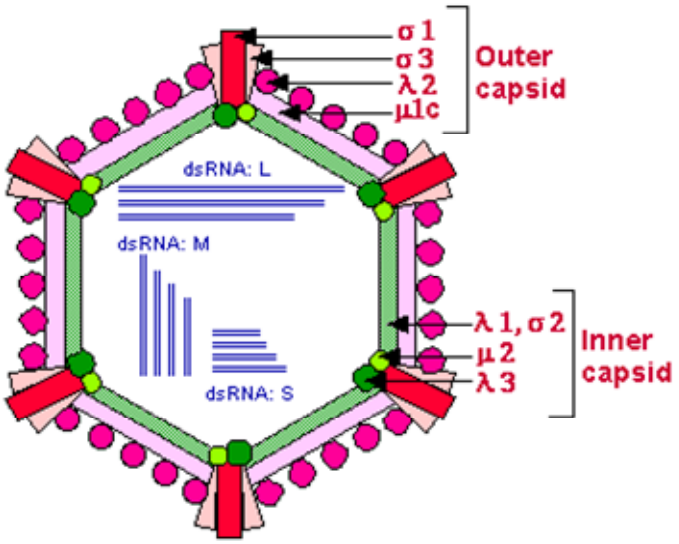

Figure 1.5: Structure of Orthoreovirus. The virion is composed of non-enveloped, icosahedral inner (proteins λ1, σ2, µ2, λ3; ~60nm diameter) and outer capsid (proteins σ1, σ3, µ1c, λ2; ~80nm diameter) . The capsid enclose the genome consisting of ten linear, segmented double-stranded RNA. L encodes proteins designated λ, M encodes proteins designated µ and S encodes proteins designated σ. From http://www-micro.msb.le.ac.uk/3035/Reoviruses.html

1.2 The vertebrate nervous system

The vertebrate nervous system is divided into the central and the peripheral nervous system. Its bigger part, the central nervous system (CNS) consists of the brain and the spinal cord. Its smaller part, the peripheral nervous system (PNS) consists of the nerves and neurons that reside or extend outside the CNS. Therefore, dorsal root ganglia belong to the PNS.

1.2.1 The central nervous system

In animals, the control center of the central nervous system is the encephalon, better known as the brain. The largest region of the mammalian brain is the telencephalon (cerebrum). Behind it lays the cerebellum, which is mainly involved in the control of movement, and is connected by thick white matter fibers (cerebellar peduncles) with the pons. Cerebrum and cerebellum each have two hemispheres. Caudal to the pons and ventral to the cerebellum, respectively, is the region called Medulla oblongata. It controls autonomic functions such as breathing and heartbeat. From here, different cranial nerves emerge, among them the hypoglossal nerve (cranial nerve XII) as well as the glossopharyngeal (cranial nerve IX) and the vagus nerve (cranial nerve X), which is of special interest in the pathogenesis of oral scrapie 263K and reovirus T3C9 in hamster. The vagus nerve contains three nuclei in the Medulla oblongata, the nucleus ambiguus, the dorsal motor nucleus and the solitary nucleus. A nucleus is a collection of neuronal cell bodies that are anatomically discrete and which typically serve a particular function. The first, the nucleus ambiguous, is a motor nucleus innervating striated muscle throughout the neck and thorax. The dorsal nucleus of the vagus is a secretomotor parasympathetic nucleus, stimulating glands, including mucus glands of the gut and gastric glands in the stomach. Finally, the solitary nucleus is a sensory nucleus that receives taste information, sensation from the back of the throat and also visceral sensation, including blood pressure receptors and stretch receptors in the gut.

1.2.2 The peripheral nervous system

The PNS is divided into the somatic and the autonomic nervous system, which in turn splits into the sympathetic and parasympathetic nervous system and is responsible for body functions like heart rate, digestion and respiration, which are done automatically and without consciousness and the ability to control. Between the central nervous system and an organ are two different nerves, separated by a ganglion, the pre- and postganglionic nerves. A ganglion is a nodule containing the nerve cell bodies of the postganglionic nerve fibers. Therefore a dorsal root ganglion is a ganglion on the dorsal root, which is attached to both sides of the spinal cord, two at each vertebra. The human spinal cord is divided into the five different regions: 8 cervical segments, 12 thoracic segments, 5 lumbar segments, 5 sacral segments and 1 coccygeal segment.

It reaches from the medulla oblongata in the brain to the filum terminale, a fibrous extension.

1.3 FTIR microspectroscopy

In general, Spectroscopy is an analytical technique arising from the interaction of a species with electromagnetic radiation, that gets either absorbed (FT-IR), scattered (FT-Raman) or emitted (XRF) by the molecules it contains.

1.3.1 Basic principles of IR spectroscopy

The electromagnetic spectrum ranges from very low energetic radio waves, with large wavelength (λ) and low frequencies (ν), to high energetic X-rays, which have small wavelength and high frequencies. Frequency and wavelength are inversely related:

$$\nu = c / \lambda \quad \text{and} \quad \lambda = c / \nu \qquad \text{Eq. 1.1}$$

(c: speed of light, 2.997925×10^8 ms^{-1})

Infrared light of the electromagnetic spectrum is located in the middle, between visible light (400-700 nm wavelength) and microwaves (10^5 – 10^7 nm wavelength). It is divided into three spectral regions: near: λ = 800 nm – 2.5 μm (ν = 12500-4000 cm^{-1}), mid: λ = 2,5 – 50 μm (ν = 4000-200 cm^{-1}) and far infrared: λ = 50 μm – 1 mm (ν = 200-10 cm^{-1}). The basic idea behind IR radiation is the fact that infrared light can cause molecules to vibrate. Depending on the atoms in the molecule, their binding forces, masses and orientation, the molecule will absorb light of specific wavelengths. This will give rise to a unique spectrum for each molecule. An absorption spectrum illustrates at what wavelength the investigated sample absorbed how much energy. Related to the wavelength, the energy of light is:

$$E = h \nu = h c / \lambda \qquad \text{Eq. 1.2}$$

(*h*: Planck's constant, 6.63×10^{-34} Js)

Vibrations can be of different nature, for a linear molecule with n atoms, there are 3n – 5 different vibrational modes, for a non linear molecule the number reduces to 3n –

6 modes. One distinguishes between symmetrical and asymmetrical stretching and different bending vibrations called rocking, scissoring, wagging and twisting (see **Figure 1.6**). Stretching vibrations usually produce stronger peaks than bending, however the bending vibrations can be useful in differentiating similar types of bonds (e.g. aromatic substitution).

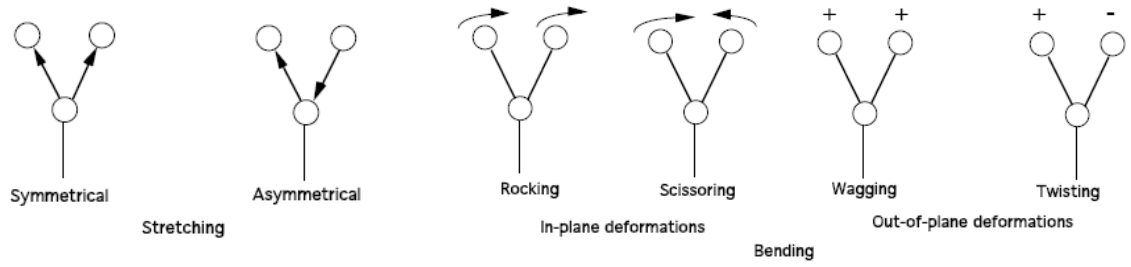

Figure 1.6: Illustration of the different vibrational modes

The harmonic oscillator, a system composed of two finite masses joined by an ideal spring, is the simplest model for the description of vibrations between two atoms. The potential energy is related to the acting force as follows:
classical picture: any transition allowed

$$E = 0.5\, kx^2 = h\,\nu \qquad \text{Eq. 1.3}$$

(*k:* force constant of the spring; *x:* displacement of the spring)

Quantum mechanical picture: The allowed transition levels for the harmonic oscillator are given by:

$$E = (n + 0.5)\, h\,\nu \qquad \text{Eq. 1.4}$$

(n: quantum number (0, 1, 2, ...))

According to equation 1.4, the lowest energy level is $E_0 = 0.5\, h\,\nu$, the next highest $E_1 = 1.5\, h\,\nu$, and so on. While this model is often sufficient to describe energy levels for lower vibrational quantum numbers, it is not exact for higher numbers. In reality, the chemical bond can not compress beyond a certain level and dissociates so that the anharmonic oscillator is a more realistic model to describe the molecules' energy levels. Here, the overall energy level expression is:

$$E_n = (n + 0.5)\, h\nu - a(n + 0.5)^2\, h\nu \qquad \text{Eq. 1.5}$$

(a: anharmonicity constant, 52.05 cm^{-1})

Harmonic Oscillator and Morse Potential are shown in **Figure 1.7**. The asymmetry of the Morse Potential illustrates the fact that it is harder to compress a bond than to pull it apart. As can be seen, the energy levels get closer with increasing quantum numbers, so that the curve approaches the dissociation energy level.

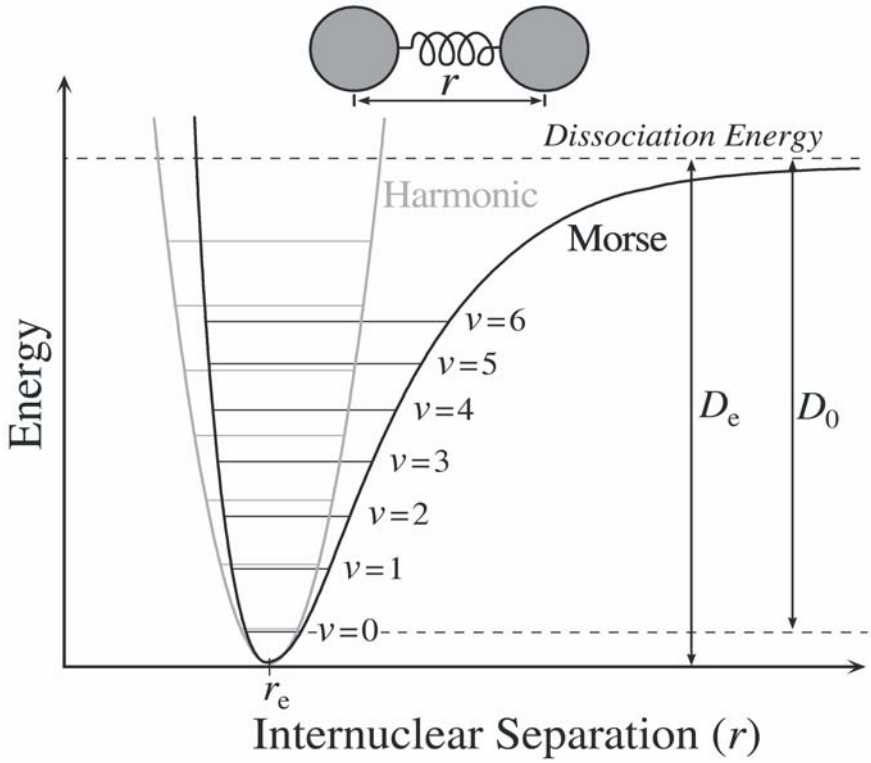

Figure 1.7: Morse (black) and harmonic oscillator potential (grey). The energy levels of the harmonic oscillator potential are evenly spaced while the Morse potential level spacing decreases as the energy approaches the dissociation energy De. The true energy required for dissociation Do is smaller than De due to the zero point energy of the lowest vibrational level (v=0).

1.3.2 The FTIR spectrometer

The heart of almost each FTIR spectrometer is the Michelson interferometer. Its basic components are a beamsplitter, a fixed and a moving mirror. Together with a detector and the IR source (typically a globar or a synchrotron), it represents the simplest FTIR spectrometer (see **Figure 1.8A**). Light produced by a globar or a synchrotron light

source separate into two individual beams by the beam splitter (a semi-reflective mirror) and travels along different light paths. At the end of these paths the light gets reflected by the fixed and moving mirrors, respectively and moves back to the beam splitter, where they interfere upon recombination. This interference is either constructive or destructive, depending on the path length travelled by each wave. The light is then focused on the sample and finally hits the detector, where an interferogram is recorded. A coupled computer transforms the interferogram (I) by Fourier transformation into a spectrum (see **Figure 1.8B**) as followed:

$$S(k\,\Delta\tilde{\upsilon}) = \Sigma\, I(n\,\Delta x)\exp(i\,2\,\pi\,nk/N) \qquad \text{Eq. 1.6}$$

(S: Signal; k: number of discrete spectrum points; n: discrete interferogram points; N: number of discrete, equidistant points)

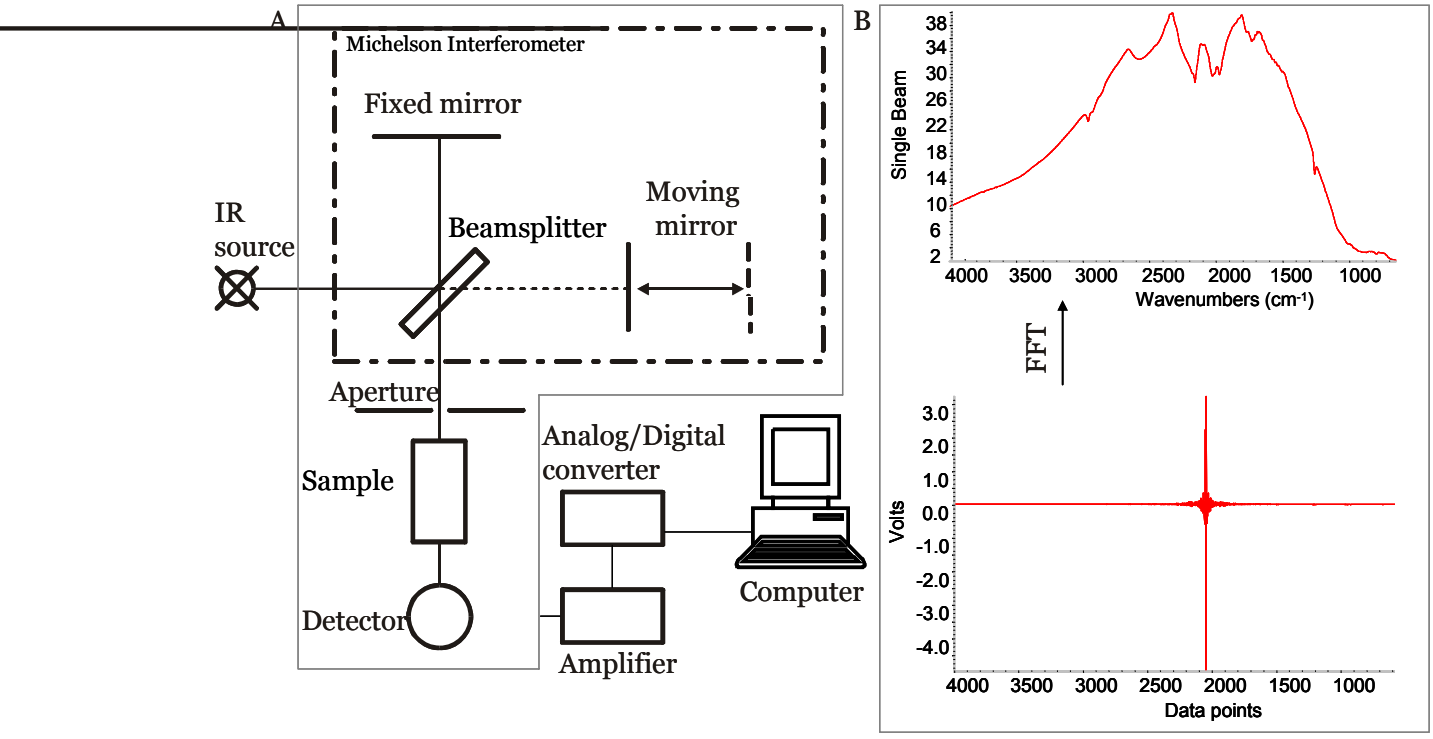

Figure 1.8: A. Schematic assembly of a spectrometer including the Michelson Interferometer. Light produced by a synchrotron or a globar (IR source) gets separated into two individual beams by the beam splitter (a semi-reflective mirror) and travels along different light paths. At the end of these paths the light gets reflected by the fixed and moving mirrors, respectively and moves back to the splitter, where they interfere upon being recombined. The light is then focused on the sample and finally hits the detector, where an interferogram is being recorded. B. Interferogram and single beam spectrum. The spectrum (top) gets calculated from the interferogram (bottom) applying Fast Fourier Transformation (FFT).

1.3.3 Advantages of FTIR versus dispersive IR spectrometer

In the 1940's, emerging dispersive IR spectrometers helped to spread the use of infrared spectroscopy as a common analytical technique for organic compound characterization in laboratories. About 20 years later, Fourier transform infrared spectrometers were developed, exhibiting several advantages over the dispersive instruments, but due to high costs, they were mainly restricted to the use in advanced research only. Three major advantages in the performance of an FTIR spectrometer over the dispersive instrument exist: the multiplex (Fellgett) advantage, the throughput (Jacquinot) advantage and the precision (Cannes) advantage.

In a dispersive spectrometer, every wavelength must be measured individually, leading to long acquisition times and the result that only one measurement scan of the sample is typically made. An interferometer in an FTIR instrument, in contrast, does not separate energy into individual frequencies. Each point in the interferogram contains information from each wavelength of light being measured, giving the advantage that many scans can be completed and combined in a shorter time. Thus, the so called multiplex or Fellgett advantage results in faster data collection of the FTIR spectrum.

The throughput (or Jacquinot) advantage describes that the energy throughput in an interferometer for the same resolution can be higher than in the dispersive spectrometer, where it is restricted by the slits. In addition, fewer mirror surfaces lead to less reflection losses and more energy reaching the detector in an FTIR spectrometer, hence providing a higher signal-to-noise ratio.

Furthermore, an FTIR spectrometer requires the use of a laser to control the velocity of the moving mirror and to time the collection of data points throughout the mirror stroke length for each scan. This laser is also used as a source of wavelength calibration within the instrument, improving accuracy and precision of the wavelength positions. This capability, called the precision or Cannes advantage, is not available on a dispersive infrared system.

1.3.4 FTIR microspectroscopy of biological tissue

An infrared spectrum displays the absorbed energy at distinct wavenumbers. A typical mid-infrared spectrum of a biological sample is given in **Figure 1.9**.

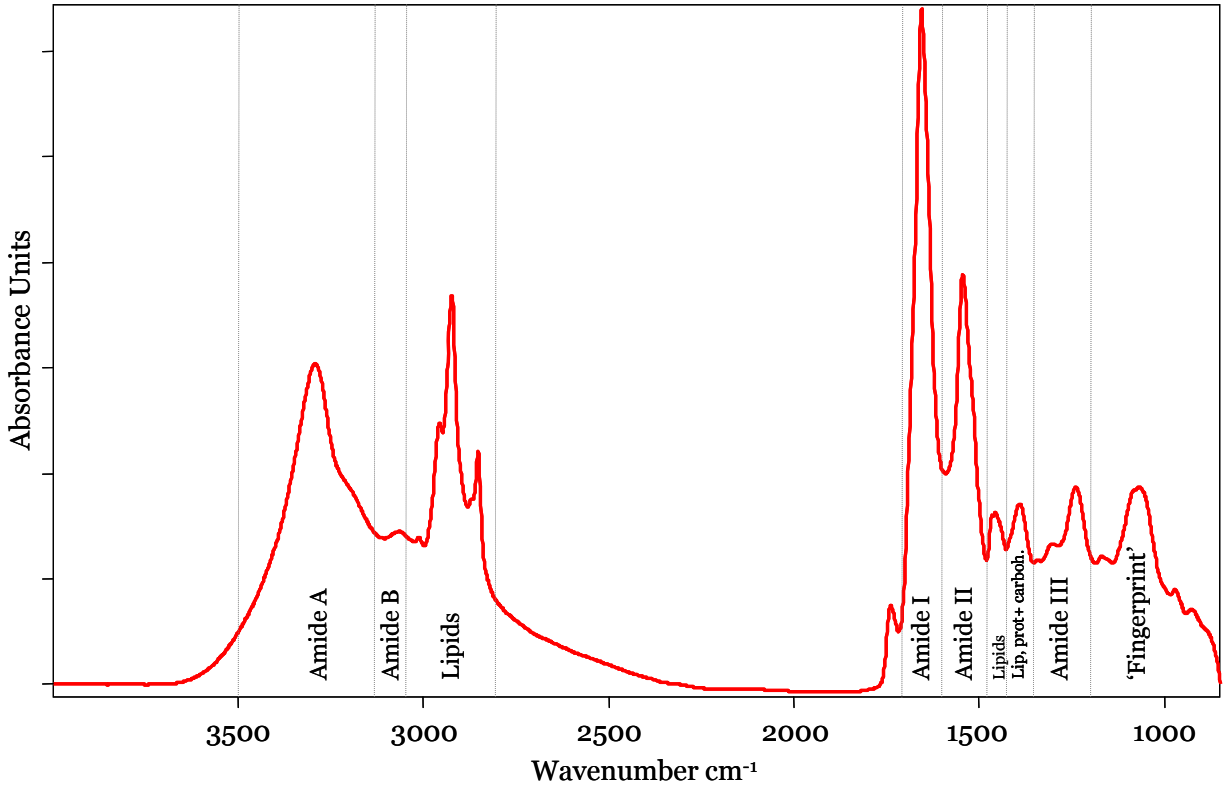

Figure 1.9: IR spectrum of a biological sample in the spectral range from 4000-900 cm^{-1}.

The intensity of a peak in an absorption spectrum is directly proportional to the concentration of the sample substance concerned, as defined by the Lambert-Beer Law:

$$A = \varepsilon \cdot b \cdot c \qquad \text{Eq. 1.7}$$

(A: Absorption maximum at a given wavelength; ε: Molar absorption coefficient; b: sample pathlength or thickness; c: sample concentration)

Upon first inspection, it can be visually divided into two regions. There are usually relatively few peaks on the left half, above 2000 cm^{-1} while they are many peaks of varying intensities on the right side, below 2000 cm^{-1}. In general the stronger the bond, the higher is the frequency of the absorbed light. Therefore, some basic rules

apply: 1. It is easier to bend a bond than to stretch or compress it, therefore bending frequencies are lower than corresponding stretching frequencies; 2. Bonds to hydrogen have higher stretching frequencies than those to heavier atoms; and 3. Single bonds have lower frequencies than double bonds which in turn have lower frequencies than triple bonds (except for bonds to hydrogen). The approximate frequency of molecular vibrations can be calculated by:

$$\nu = \frac{1}{2\pi c}\sqrt{\frac{k}{\mu}} \qquad \text{Eq. 1.8}$$

(σ: wavenumber; c: speed of light; *k*: bond force constant; μ: reduced mass)

and

$$\mu = \frac{m_1 m_2}{m_1 + m_2} \qquad \text{Eq. 1.9}$$

(μ: reduced mass; m_1: mass for atom 1 (g/atom); m_2: mass for atom 2 (g/atom)

Therefore, σ (C-C) ≈ 1185 cm^{-1} (k = 5 x 10^5 dynes/cm), σ (C=C) ≈ 1676 cm^{-1} (k = 1 x 10^6 dynes/cm) and σ (C≡C) ≈ 2053 cm^{-1} (k = 1.5 x 10^5 dynes/cm). **Table 1.2** gives a summery of functional group absorbences.

Table 1.2: IR band assignment of biological molecules [(Fabian & Schultz, 2000; Fabian & Mäntele, 2002; Yu & Irudayaraj, 2005; Chalmers & Griffith, 2002)]

Absorption band (cm^{-1})	**Chemical compound**	**Assignment**
~3300	proteins	N-H stretching vibration (Amide A)
~3100	proteins	N-H stretching vibration (Amide B)
~3030	lipids	=C-H stretching in alkenes
2955 and 2872	lipids, proteins, carbohydrates, nucleic acids	asymmetric and symmetric C-H stretching vibration from CH_3 groups
2923 and 2853	lipids, proteins, carbohydrates, nucleic acids	asymmetric and symmetric C-H stretching vibration from CH_2 groups
1741	phospholipids, thymine, uracil	C=O stretching vibration of esters
~1550	proteins	N-H bending, C-H stretching, C-O bending, C-C and N-C stretching vibrations (Amide II)
~1515	proteins	tyrosine
~1467	lipids, proteins, nucleic acids	symmetric C-H scissoring of $-CH_2$
~1454	lipids, proteins	asymmetric C-H scissoring of $-CH_3$
~1400	fatty acids, amino acid side chains	C=O stretching vibrations of $-COO^-$
~1390	proteins, lipids	symmetric C-H deformation of $-CH_3$
~1310-1200	proteins	C-H/N-H deformation (Amide III)
~1250-1220 (1235)	nucleic acids, phospholipids	asymmetric P=O stretching vibrations in PO_2^-
~1200-900	polysaccharides	C-O-P and C-O-C stretching vibrations, ring vibrations
~1173 and 1154	carbohydrates	symmetric C-O stretching coupled to C-O-H bending
~1085	nucleic acids (DNA), phospholipids	symmetric P=O stretching in PO_2^-, CO-O-C symmetric stretching vibrations
~1070	lipids	symmetric CO-O-C stretching vibration
~1041 and 1055	carbohydrates	symmetric C-O-C stretching vibration
~1023	carbohydrates	symmetric C-O stretching vibration
900-800	nucleotides	C=C, C=N, C-H in ring structure
700	proteins, lipids, nucleic acids	$-CH_2$ rocking

An infrared spectrum of a biological sample is composed of characteristic absorption bands originating from all molecules it contains, including proteins, lipids, nucleic acids, and carbohydrates. Since the combination of all molecular parameters (structure, composition, and/or interactions) in a specific tissue structure, cell type, or part of a cell is unique, FTIR microspectroscopy, which provides fingerprint-like information, is capable of characterizing distinct tissue structures (Wetzel & LeVine, 1999). Over the past years, this has been shown for many types of tissues, mainly with the goal of developing efficient diagnostic procedures to detect tissue pathologies such as in the cervix (Romeo *et al.*, 2002; Chiriboga *et al.*, 1998), brain (Choo *et al.*, 1996; Kneipp *et al.*, 2000), colon (Lasch *et al.*, 2004; Lasch & Naumann, 1998), breast (Zhang *et al.*, 2003), heart (Wang *et al.*, 2005b), and also of individual normal and cancerous cells (Diem *et al.*, 2002). Brain tissue has been studied by vibrational spectroscopic methods for quite a long time for several reasons. One reason is the extraordinary high IR spectral contrast between white and gray matter of the brain (e.g. (LeVine & Wetzel, 1993; Choo *et al.*, 1993)), facilitating the development of spectral imaging methodologies on tissues (Lewis *et al.*, 1996). Over the past decade it was shown that also less obvious molecular differences (e.g. within grey matter brain structures and even sub-structures that are not easily identified by histology) can be used for IR based differentiation in the cerebellum and the nuclei of the cranial nerves (Kneipp *et al.*, 2000; Lester *et al.*, 1998; Kneipp *et al.*, 2002). The second, and main reason for FTIR studies on brain tissue is that, together with Raman spectroscopy, it is possibly the only way to elucidate the complex molecular background of some severe pathologies of the central nervous system (CNS) in situ on the tissue. No labels, stains or dyes are required for IR and it is a non-destructive, sensitive and fast tool, properties that cannot be achieved by other, either antibody/label- or purification-based methods. Among the investigated pathologies in brain tissues are multiple sclerosis, where lesions in white matter (the myelin sheaths of neurons) were detected (Choo *et al.*, 1993) and Alzheimer's disease, which is characterized by disease-specific, plaque-like protein accumulations, that can be detected by distinct changes in the amide I region of an IR spectrum (Choo *et al.*, 1996). This region of the vibrational spectrum gives information about the secondary structure of a protein in the investigated sample. Assignment of amide I band components to e.g. β-pleated sheets or α-helical structures is given in table x. This region between 1600 and 1700 cm^{-1}

mainly represents the carbonyl stretching vibration of the peptides backbone. It is a sensitive marker of protein secondary structures because the vibrational frequency of each C=O bond depends on hydrogen bonding and the interaction between the amide units, both of which are influenced by the secondary structure. In addition to the most prominent, amide I band, there are eight other amide bands, called amide A, amide B and amide II-VII.

Table 1.3: Assignment of IR absorption bands (cm^{-1}) to different secondary structures of proteins determined by measurements in H_2O (from: (Dong *et al.*, 1990; Barth & Zscherp, 2002; Fabian & Mäntele, 2002))

Amide I Secondary Structure Assignments	
~1615-1625	Aggregated strands (intermolecular β-sheets)
~1625–1640	β-sheet
~1650-1660	Disordered
~1650-1665	α –helix
various bands between 1650 and 1690	Turns and loops
~1680-1695	anti-parallel β-sheet

1.4 X-Ray fluorescence microprobe

X-rays, discovered by Röntgen in 1878, represent the region of the electromagnetic spectrum with wavelengths ranging from 10 to 0.01 nm. X-ray fluorescence (XRF) microprobe is a non-destructive method of measuring the elemental composition of a material by irradiating a sample with high energy photons and observing the resulting characteristic x-ray fluorescence emitted by the sample. When the sample is exposed to x-rays, the high energy photons are absorbed. If the energy of the photon is greater than the binding energy of an inner shell electron, the electron is ejected, creating a vacancy. Since this vacancy is an unstable condition for the atom, an electron from an outer orbit will then fall into the shell of the missing electron, which is called

"relaxation". Since outer shell electrons are more energetic than inner shell electrons, the relocated electron has an excess of energy that is emitted as characteristic "fluorescence" x-ray, which is unique to the composition of the sample. In most cases the innermost K and L shells are involved in XRF detection (see **Figure 1.10**).

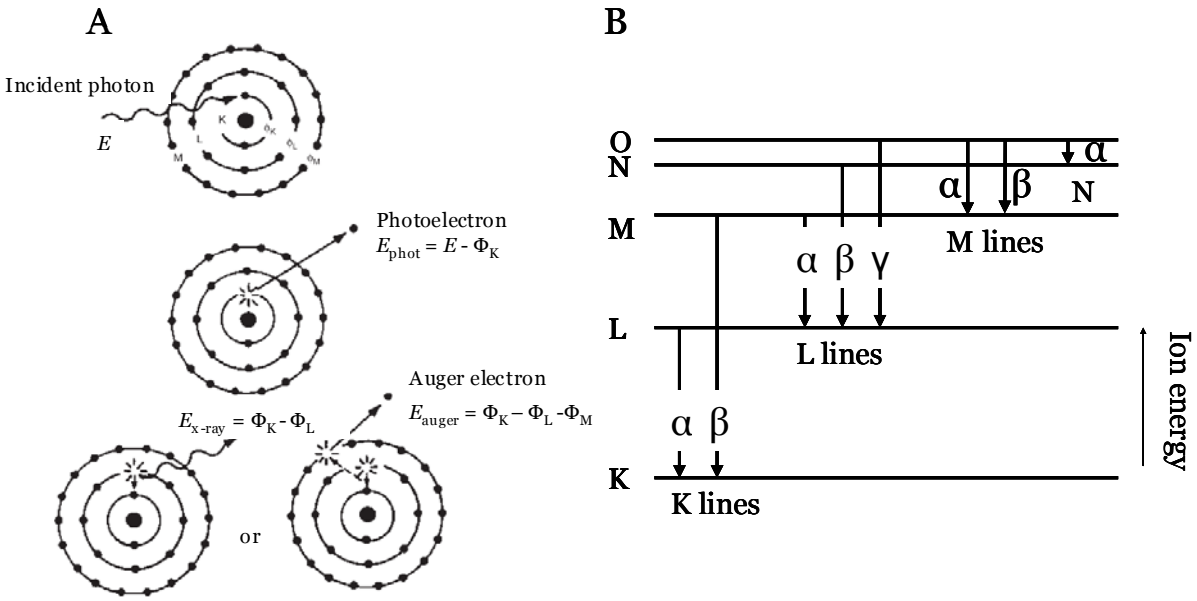

Figure 1.10: A. Principles of XRF. Photoelectric ionization can be followed by either radiative relaxation, causing the emission of characteristic fluorescent X-rays or non-radiative relaxation,involving the emission of Auger electrons. From (Janssens, 2004) B. Classification of K, L, M, N and O shells.

While the elements in the sample are detected by characteristic fluorescence wavelengths, their concentration is determined by the intensity of the fluorescence emission peaks. The resulting spectrum, recorded by an energy-dispersive detector, is graphed as intensity vs. energy. **Figure 1.11** shows a typical XRF spectrum of nervous tissue measured at beamline X26a at the National Synchrotron Light Source in Upton, NY. The characteristic x-rays are labelled as K, L, M or N to denote the shells they originated from. Another designation alpha (α), beta (β) or gamma (γ) is made to mark the x-rays that originated from the transitions of electrons from higher shells. Hence, a K_α x-ray is produced from a transition of an electron from the L to K shell, and a K_β x-ray from a transition of an electron from the M to a K shell, and so on (compare **Figure 1.10**). To denote transitions of electrons from orbits into the same lower shell, α_1, α_2 or β_1, β_2 is used. By using a synchrotron x-ray source, monochromatic x-rays can be produced and focused to small spots so that trace metal

content can be obtained on the sub-micrometer scale and parts-per-million concentration level can be detected.

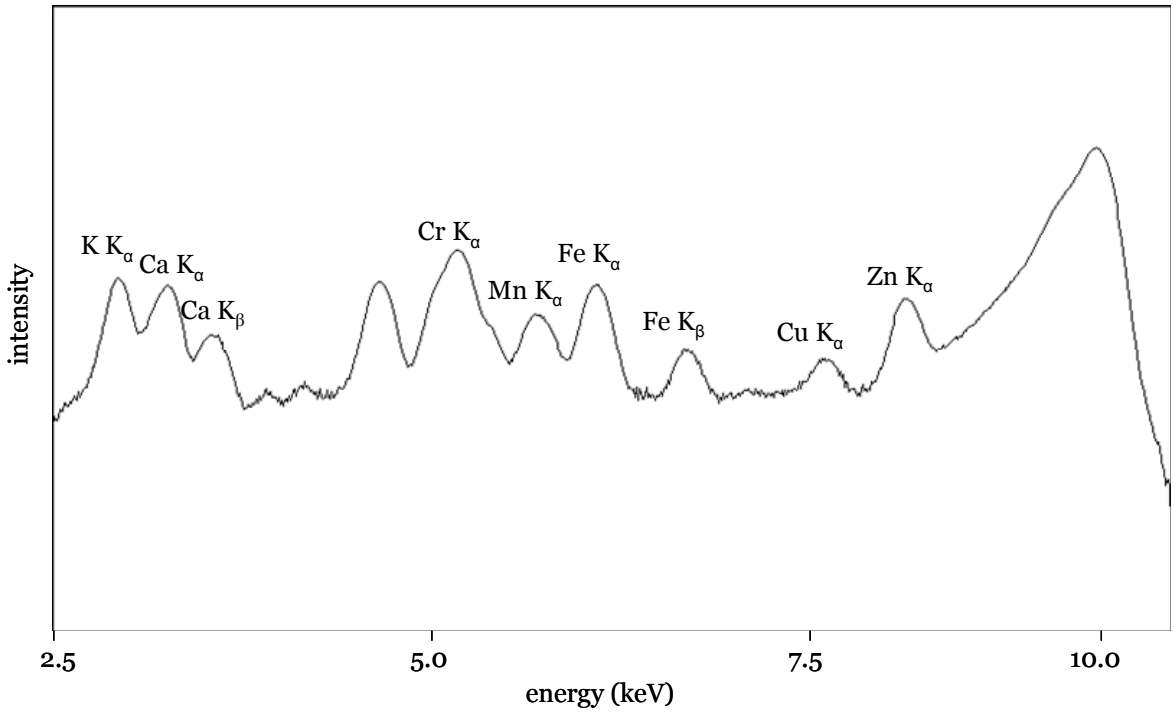

Figure 1.11: Typical XRF microprobe spectrum. The observed peaks are labeled according to the involved atoms and shells.

1.5 Previous FTIRMS studies on scrapie infected nervous tissue

Pilot studies on scrapie infected nervous tissue investigated with FTIRMS were performed previously in our lab and served as motivation for the experiments performed in this thesis and described in the next chapter. They will be presented briefly in this chapter.

1.5.1 FTIR-based detection of pathological changes in scrapie-infected hamsters

The investigation of TSE in situ in nervous tissue is of basic interest, since the complex molecular background of the known morphological and ultrastructural changes in the course of the disease is far from being fully understood except for some selected

parameters such as the PrP^{Sc} accumulation. In addition, the need for fast and efficient detection methods for prion diseases in the area of food safety gave the motivation to study prion-affected tissues by FTIR spectroscopy. Early FTIR microspectroscopic experiments on orally scrapie infected terminally diseased hamsters revealed molecular differences between the infected and control animals based on spectral changes detected in specific regions of the cerebellum (Stratum moleculare, Stratum ganglionare, Stratum granulosum and Substantia alba) (Kneipp *et al.*, 2000). It was observed that FTIR spectral differences between the various cerebellar histological structures were much larger than those between control and infected animals. It was therefore crucial to compare spectra of infected and uninfected material from exactly the same tissue substructures. Similar observations were made in FTIR-microspectroscopic studies of the medulla oblongata and of the cerebellar nuclei (Kneipp *et al.*, 2002). While clear spectral distinction between scrapie infected, homogenized medulla oblongata and pons tissue was possible for the terminal stage (Kneipp *et al.*, 2000), it turned out to be difficult to differentiate in earlier (pre-clinical) stages. However, the comparison of spectra from specific nuclei in the medulla oblongata enabled identification of disease-specific spectral patterns also in the pre-clinical stage (Kneipp *et al.*, 2002). It was demonstrated that the spectra needed to be sorted according to the anatomical substructures before separating "diseased" and "non-diseased" spectral patterns (Kneipp *et al.*, 2000). It was only this method that avoided mixing up disease-specific and morphology-specific spectral differences. To attain classification of brain-structure specific spectral patterns, univariate as well as multivariate analysis and image reconstruction techniques were used. In the case of the cerebellum, principal component analysis (PCA) was applied. Using this PCA approach, the four histologically defined layers S. ganglionare, S. moleculare, S. granulosum and S. alba could not only be separated to four distinct clusters, but also into substructures that were not distinguishable by common staining methods such as cresyl violet or hematoxylin/eosin staining (Kneipp *et al.*, 2000). In a second step, hierarchical cluster analysis was performed on single pixel spectra of the latter three histological structures from scrapie-infected and control hamsters revealing a clear separation between spectra of infected and uninfected animals. In analyzing the spectra, the protein/lipid ratio turned out to be useful to distinguish spectra of the nuclei of the cranial nerves from the surrounding tissue (high protein content of the nuclei and high lipid content of the adjacent areas, see **Figure 1.15A**)

in the medulla oblongata. The protein/lipid ratio, however, was able to distinguish only between the gray and white matter in hippocampus (Dubois *et al.*, 2003). The DMNV and solitary tract nucleus could further be separated from the hypoglossal nucleus in a cluster analysis-based IR imaging procedure (Kneipp *et al.*, 2002). Spectral changes due to the scrapie infection varied in extent and quality for the different brain structures. In the cerebellum, to give an example, alterations could be detected in the spectral region between 2800 and 3050 cm^{-1} (dominated by absorption bands of the asymmetric and symmetric C–H stretching vibrations of $>CH_2$ and $>CH_3$ methylene groups) and in the fingerprint region between 1000 and 1300 cm^{-1}. Changes in the CH-stretching region led to the assumption that an altered protein composition of the membranous system influenced the membrane state-of-order via lipid–protein-interactions. Changes in the fingerprint region (1000–1300 cm^{-1}) were not only observed in the area of the cerebellum, but also in the nuclei of the medulla oblongata (Kneipp *et al.*, 2002). In fact, the earliest spectral changes that were observed in a time course study of the disease progression in this part of the brain occured 90 days post-infection in the DMNV. These alterations were observed in the spectral region between 1040 and 1060 cm^{-1} (see **Figure 1.15D**) and were shown to be indicative of an altered composition and/ or structure of carbohydrates (sugar moieties of nucleic acids or changed content of metabolic sugar molecules in the cell such as glucose). The early stage of the disease has been characterized by microvacuolation (Marsh & Kimberlin, 1975), membrane proliferation, structural and functional damage of mitochondria (Choi *et al.*, 1998) and DNA decomposition during apoptosis and/or a changed RNA content as the result of up- or down-regulation of genes (Riemer *et al.*, 2000). By cluster analyses on DMNV spectra from diseased and control animals at 90 and 120 days post infection (dpi), respectively, spectra from infected animals could be clearly separated from controls (see **Figure 1.12C**). Worth mentioning is the fact that 90 dpi spectra and 120 dpi spectra did not form two distinct classes, indicating that progression of molecular changes is individually variable. The fact that the earliest spectral changes were reported to occur in the DMNV is in accordance with earlier pathogenesis studies which used immunohistology of the misfolded PrPSc as the disease marker (McBride *et al.*, 2001). Interestingly, although the disease is characterized by the accumulation of a misfolded protein, no statistically significant differences in the amide I region were found in any of the data sets acquired with standard FTIR microscopes equipped with conventional

globar sources and single-element detectors (Kneipp *et al.*, 2002; Dubois *et al.*, 2003). This observation holds true even for anatomical structures known to show early and intense PrP^{Sc} accumulations in the 263K hamster model (DMNV). Since PrP^{Sc} accounts for less than 0.1% of all proteins in the diseased brain tissue in the terminal stage (Beekes *et al.*, 1996), the local protein concentration was probably too low to be detected at the given spatial resolution. An FTIR spectrum is always the sum of individual spectral components from the structures under investigation. Thus, the acquisition of high quality FTIR microspectra from the smallest possible sample volume is indispensable for detection of small-sized accumulations of protein aggregats such as PrP^{Sc} in the brain. As has been illustrated recently, this "optical dilution effect" makes it impossible to detect microdisperse PrP^{Sc} aggregates even with apertures as small as 30×30 μm^2 (Kneipp *et al.*, 2004).

1.5.2 FTIR microspectroscopy of dorsal root ganglia utilizing a synchrotron IR light source

In a recent pilot study, spectra from dorsal root ganglia of 263K hamsters were acquired using a synchrotron, which provided a spatial resolution approaching the diffraction limit of mid-infrared light (Kneipp *et al.*, 2003). Thirty-one neurons from infected and thirty-two neurons from control hamster were investigated, respectively. Although the diffraction limit of IR light is ~6 μm at 1650 cm^{-1}, which is still bigger than the size of typical PrP^{Sc} aggregates in 263K, differences associated with PrP^{Sc} deposition could be detected in the amide I region with aperture sizes of 10 μm (Kneipp *et al.*, 2003). Results showed that the peak at around 1657 cm^{-1}, associated with α-helical protein structures, decreased and shifted to lower frequencies in spectra from infected animals, and the peak at ~1637 cm^{-1} increased. In some spectra from infected hamsters, an additional peak at around 1631 cm^{-1} also appeared. This argued for a higher β-sheet and lower α-helix content of the proteins in the investigated areas. Similarly small sampling volumes were reported in an experiment using a focal plane array detector to study the hippocampus of 263K-infected hamsters and yielded some spectra with a changed amide I contour that could indicate diffuse protein deposits (Dubois *et al.*, 2003). More recent synchrotron FTIR spectroscopic studies supporting the results of the initial study have been extended to a larger number of animals (Wang *et al.*, 2005a).

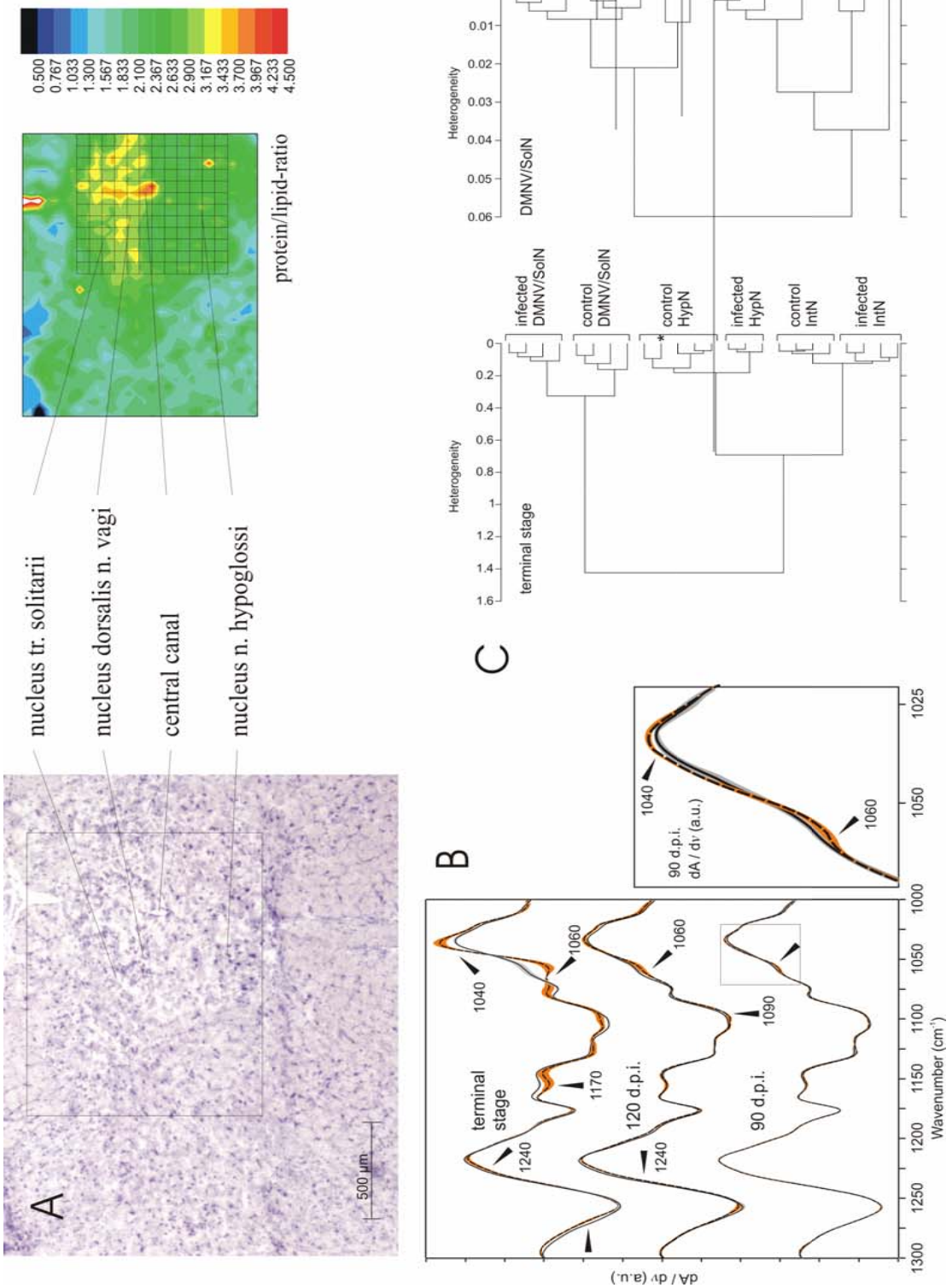
A
nucleus tr. solitarii
nucleus dorsalis n. vagi
central canal
nucleus n. hypoglossi
500 µm
protein/lipid-ratio
0.500
0.767
1.033
1.300
1.567
1.833
2.100
2.367
2.633
2.900
3.167
3.433
3.700
3.967
4.233
4.500
B
terminal stage
120 d.p.i.
90 d.p.i.
1040
1060
1170
1240
1090
90 d.p.i.
dA / dν (a.u.)
Wavenumber (cm-1)
C
Heterogeneity
terminal stage
infected DMNV/SolN
control DMNV/SolN
control HypN
infected HypN
control IntN
infected IntN
D
Heterogeneity
DMNV/SolN
controls (90 d.p.i. & 120 d.p.i.)
infected (90 d.p.i.)
infected (120 d.p.i.)

Figure 1.12: (A) FTIR overview image based on the protein/lipid ratio calculated from the FTIR spectra (right) and visible micrograph of the cresyl fast violet stained adjacent tissue section (left; scale bar, 500 μm) for orientation in the medulla oblongata, containing the nuclei of the solitary tract, the DMNVand the nucleus of the HypN. The nuclei can be distinguished from the surrounding white matter by their high protein content shown as yellow and red areas in the right picture. The inset in the left photomicrograph indicates the tissue area investigated by IR imaging. The grids in the IR map show areas of detailed measurements that were performed for additional investigations. (B) Normalized first derivatives of average spectra of DMNV/SolN at three stages of the disease, each obtained from single spectra of four scrapie-infected hamsters (dashed lines) and four control hamsters (solid lines) with their standard deviations (dark, infected; light, normal controls) displayed over the frequency range 1000–1300 cm^{-1}. Arrowheads indicate differences between spectra. The inset displays the spectral region containing subtle differences between the averages at 90 d.p.i. (C) Cluster analyses of spectra of the DMNV/SolN, HypN, and IntN of four terminally diseased and four control animals using the spectral information between 950 and 1480 cm^{-1}. The spectrum of the HypN of one of the infected hamsters was grouped with the controls (asterisk). (D) Cluster analysis of spectra from the DMNV/SolN of eight infected hamsters (four 120 d.p.i. and four 90 d.p.i.) and the corresponding eight controls based on the spectral information between 1025 and 1050 cm^{-1}. All first-derivative spectra were normalized over the frequency range 1000–1300 cm^{-1}. One infected individual at 120 d.p.i. appears in the 90 d.p.i. group (asterisk). Adapted from (Kneipp, 2002). Copyright 2002 by the Society für Neuroscience.

1.6 Aims

The molecular events underlying the pathogenesis of scrapie especially at the early stages are still poorly understood. To date, the majority of studies on this topic have been performed on terminally ill animals and much less is known about the initial cellular processes that lead to the clinical signs of the disease. Thus, the main goal of this thesis was to examine the chemical composition of scrapie infected nervous tissue at pre-clinical time points in order to investigate prion-induced molecular differences.

Specific Aim 1. Scrapie pathogenesis is associated with the accumulation of the misfolded prion protein, PrP^{Sc}, in infected cells, especially at late stages of the disease. However, much less is known about protein-related changes at pre-clinical time points. To address this, we have performed a time course study of scrapie infected hamsters to examine the changes in protein structure, composition, and distribution over the course of the disease from pre-clinical to terminal stages using a combination of immunostaining and infrared micro-spectroscopic imaging. In order to obtain the highest spatial resolution and sensitivity, a synchrotron infrared source was used.

Hypothesis: For this specific aim, we hypothesized that DRG of scrapie-infected animals exhibit alterations in β-sheet content over the course of the disease, starting from a similar protein composition as in controls at early stages to increasing amounts of β-sheet content towards the end of the disease.

Specific Aim 2. Earlier studies of scrapie-infected DMNV in the brain (Kneipp *et al.*, 2002; Kneipp, 2001) demonstrated that non-protein chemical changes were also observed in pre-clinical time point as early as 90 days post infection (dpi). In addition, early scrapie-induced changes were related to alterations in the membrane system, such as microvacuolation (Marsh & Kimberlin, 1975), membrane prolifereation and structural and functional damage of mitochondria (Choi *et al.*, 1998). In this study, we have taken advantage of the high spatial resolution and sensitivity of synchrotron infrared microspectroscopy to investigate subcellular compositional changes of major cellular biomolecules (e.g. lipid, nucleic acids, carbohydrates) at an early time point, i.e. 70 dpi.

Hypothesis: For this specific aim, we hypothesized that the DMNV of 70 dpi scrapie-infected animals exhibit spectral alterations similar to those detected by Kneipp *et al.*, although to a lesser extent. In addition, alterations in lipid content or composition, indicative of early scrapie-induced changes in the membrane system, are likely to be expected.

Specific Aim 3. It is known that TSEs are related with perturbations in metal homeostases, but little is known about the exact involvement of metal ions in these diseases. Specifically for scrapie, it has been suggested that the normal prion protein binds copper and may play a role in copper homeostasis (Stockel *et al.*, 1998; Burns *et al.*, 2003; Millhauser, 2004; Burns *et al.*, 2002; Brown *et al.*, 2001; Brown *et al.*, 1997a; Viles *et al.*, 1999; Hornshaw *et al.*, 1995). Additionally, the prion protein was shown to induce apoptosis, which in turn triggers the release of calcium from its intracellular strores (Krebs *et al.*, 2007; Kawahara *et al.*, 2000; Florio *et al.*, 1996; Whatley *et al.*, 1995; Kristensson *et al.*, 1993; Grebinyk *et al.*, 2004; Beaver & Waring, 1994). In order to investigate the involvement of copper and other trace metals (e.g. Fe, Mn, Zn) in the disease, we have examined the metal content and distribution from the same time course study described in Specific Aim 1 using synchrotron x-ray fluorescence (SXRF) microprobe.

Hypothesis: For this specific aim, we hypothesized that scrapie-infected hamster DRG exhibit alterations in metal content and distribution, such as copper, iron and zinc at the terminal stage of the disease. Furthermore, alterations in e.g.

calcium can potentially be detected at pre-clinical time points, reflecting early apoptotic prion-induced events.

Specific Aim 4. While compositional changes were observed in Specific Aims 1-3 and in earlier studies (Kneipp *et al.*, 2000; Kneipp *et al.*, 2002; Kneipp, 2001), their specificity to scrapie infection was still unclear. 263K and ME7 are two different scrapie strains which differ in glycosylation pattern, incubation time, microstructural accumulation of PrP^{Sc} and infection of animals. Thus, a similar set of experiments was performed on hamster brain infected by Reovirus T3C9, another neurological disease, and compared to the 263K results. Finally, DRG of scrapie-ME7 infected animals were compared to those of 263K infected hamsters.

Hypothesis: For this specific aim, we hypothesized that 263K infected DMNV in the brain and neurons of DRG exhibit unique spectral patterns that can not be found in the DMNV of Reovirus infected brain nor in neurons of ME7 infected DRG.